

Nanoscale

Accepted Manuscript



This is an *Accepted Manuscript*, which has been through the Royal Society of Chemistry peer review process and has been accepted for publication.

Accepted Manuscripts are published online shortly after acceptance, before technical editing, formatting and proof reading. Using this free service, authors can make their results available to the community, in citable form, before we publish the edited article. We will replace this *Accepted Manuscript* with the edited and formatted *Advance Article* as soon as it is available.

You can find more information about *Accepted Manuscripts* in the [Information for Authors](#).

Please note that technical editing may introduce minor changes to the text and/or graphics, which may alter content. The journal's standard [Terms & Conditions](#) and the [Ethical guidelines](#) still apply. In no event shall the Royal Society of Chemistry be held responsible for any errors or omissions in this *Accepted Manuscript* or any consequences arising from the use of any information it contains.



Engineering microencapsulation of highly catalytic gold nanoclusters for an extreme thermal stability

Ana Sousa-Castillo,^a Mathilde Gauthier,^a Raul Arenal,^{b,c} Moisés Pérez-Lorenzo,^{*a} and Miguel A. Correa-Duarte^{*a}

Received 00th January 20xx,
Accepted 00th January 20xx

DOI: 10.1039/x0xx00000x

www.rsc.org/

A synthetic strategy for the microencapsulation of ultra-small gold nanoparticles toward the development of a novel nanoreactor is reported. In this case, it is shown that the catalytic activity of Au nanoclusters as small as 0.8 nm remains unaffected after exposure to a thermal treatment of up to 800 °C in air. This is accomplished through the deposition and further coating of the gold nanoparticles in a void/silica/Au/silica configuration where the nature of the alternate shells can be tuned regardless of each other's porosity and the size of the embedded metal nanoparticles. Such spatial confinement suppresses the growth of the gold nanoclusters and thus, preserves their catalytic properties. In this way, a remarkable compromise between the immobilization and the accessibility to the metal nanocatalyst can be met. Furthermore, these nanoreactors are found to be colloiddally stable under simulated body fluids which also makes them suitable for biomedical applications. The implementation of hollow nanoreactors containing highly dispersed and immobilized but accessible ultra-small metal nanoparticles constitutes a promising alternative in the search for model catalysts stable under realistic technical conditions.

^a Department of Physical Chemistry, Biomedical Research Center (CINBIO), and Institute of Biomedical Research of Ourense-Pontevedra-Vigo (IBI), Universidade de Vigo, 36310 Vigo, Spain. E-mail: moisespl@uvigo.es; macorrea@uvigo.es

^b Laboratorio de Microscopías Avanzadas (LMA), Instituto de Nanociencia de Aragón (INA), Universidad de Zaragoza, 50018 Zaragoza, Spain

^c ARAID Foundation, 50018 Zaragoza, Spain

† Electronic Supplementary Information (ESI) available: Synthetic procedures, catalytic experiments and characterization. See DOI: 10.1039/x0xx00000x

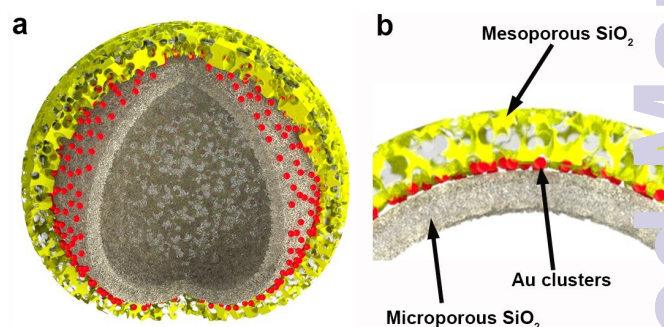
Introduction

Small gold nanoparticles (AuNPs) finely dispersed on solid supports are well-known for being active and highly selective catalysts in a large variety of organic reactions.^{1–4} In this regard, these materials has been usually applied in hydrogenation of alkenes, aromatic compounds and nitro groups as well as oxidation of alkenes, alcohols and amines. Coupling, cyclization and carbonylation reactions are also among the processes where these materials has been successfully used. Nevertheless, despite their excellent performance a major drawback arises in the application of supported AuNPs at moderate-to-high temperatures given their tendency to aggregate into fewer and larger particles.⁵ This nanoparticle growth, especially acute in the sub-2 nm regime, is usually referred to as sintering or thermal deactivation and leads to a remarkable loss of catalytic activity.⁶ In this context, it is worth stressing that elevated temperatures are commonly an essential requirement for conducting reactions in the presence of supported gold catalysts. High temperatures are used with colloidal AuNPs deposited on solid substrates so as to remove the organic capping agent (either a surfactant or a polymer) thereby allowing reactants to access to the catalyst active sites.⁷ Calcination procedures play also an important role in the induction of stronger metal-support interactions leading to enhanced activities. This is especially useful when dealing with reducible metal oxides supports.⁸ Likewise, many industrially relevant processes are driven under high-energy demanding conditions in the presence of gold nanoparticle-based materials.³ Therefore, the design of model catalysts stable at realistic technical conditions is of crucial importance in order to preserve the catalytic properties of metal nanoparticles, which in the end will endow them with a longer cycle life.

Thermal stabilization becomes especially challenging in the case of gold nanoparticles since only a few studies have proven to efficiently preserve their catalytic activity at elevated temperatures.^{3,9} As an example, this drawback has been recently evidenced by infiltrating AuNPs into mesoporous TiO₂ thin films through an impregnation-reduction method.¹⁰ In this approach, it is demonstrated that particle coarsening may start through ripening and particle migration at temperatures below 200 °C. Similarly, aggregation of small AuNPs inside ordered mesoporous silica channels has been recently reported.¹¹ In order to circumvent this problem, coating of preformed catalytic nanoparticles with a protecting shell has been proven an efficient strategy. A notable example of this approach consists of the encapsulation of gold or platinum nanoparticles into mesoporous silica shells.^{12,13} However, the immobilization of ultra-small metal nanocatalysts at high temperatures still constitutes a great challenge. This is particularly complex when the metal nanoclusters are smaller than the pore size of their own protecting layer, which allow a better access of the reactants to the catalyst surface but lower sintering-resistant capabilities.

To overcome the above-mentioned limitations, the present work describes the microencapsulation of 0.8–1.2 nm Au clusters embedded at the interface between two different silica layers that give rise to the final capsular structure (Scheme 1). At this point, it is worth to highlight that the porosity of the alternate silica layers can be modified regardless of each other's porosity. This synthetic

versatility has been exploited to show the extreme thermal stability of metal clusters smaller than the pores of the outer silica layer (3 nm). In this line, the thermal stability of these small AuNPs has been studied by using an electron transfer reaction as a chemical probe, revealing an outstanding stability of the nanoparticles at temperatures as high as 800 °C. These results clearly confirm the role played by the two silica layers as physical barrier to prevent Au nanoparticles movement, aggregation, and detachment from the support into the bulk solution. All these results has been compared to silica-embedded 14 and 2.6 nm AuNPs. Additionally, these capsular nanocomposites show a notable dispersibility and stability in various solvents including simulated body fluids (SBF) which shows the potential of these nanostructures for biomedical applications.



Scheme 1. Illustration of (a) gold nanocluster-containing hybrid capsular nanocomposite; and (b) detail of the embedment of the metal nanoparticles between silica shells of different porosity.

Results and discussion

As a preliminary step toward the implementation of the void/silica/Au/silica architectures as nanoreactors, the thermal stability of different sized AuNPs was assessed through the use of their silica/Au/silica core-shell counterparts. In the case of 0.8–1.2 nm Au clusters, silica beads were functionalized with a positively charged amino-rich polyelectrolyte (poly(allylamine hydrochloride), PAH). Then, the beads were introduced in a solution containing the catalyst precursor (HAuCl₄) followed by a citrate-mediated reduction (Figure 1e).¹⁴ It is worth to underline that while amino groups favor the reduction of Au³⁺ ions acting also as binding sites for gold, an adequate concentration of citrate serves as both reducing and stabilizing agent. In the case of the pre-synthesized 14 and 2.6 nm AuNPs, produced as described elsewhere,^{15,16} PAH functionalized silica beads were also used to afford the corresponding SiO₂/14 and 2.6 nm AuNPs composites (Figure 1a and 1c, respectively). In all cases, the resulting SiO₂/AuNP nanocomposites were rinsed in order to remove the excess of unreacted species by successive centrifugation/redispersion cycles spinning at 3000 rpm for 20 min and redispersing in pure water by stirring. Then, a SiO₂ ad-layer was added to yield a SiO₂/AuNPs/SiO₂ structure (Figure 1b, 1d, and 1f). This silica shell was aimed to further enhance the stability of the silica-supported AuNPs by acting as a physical shield. In this way, the spatial confinement of the AuNPs should suppress their growth and therefore, preserve

their catalytic properties. Furthermore, the porous nature of the shell may allow an efficient exchange of reactants and products. In this case, the high surface area of silica coatings favors the

adsorption of reagents and thus, enriches the presence of reactants around the catalyst promoting chemical reactions.¹⁷

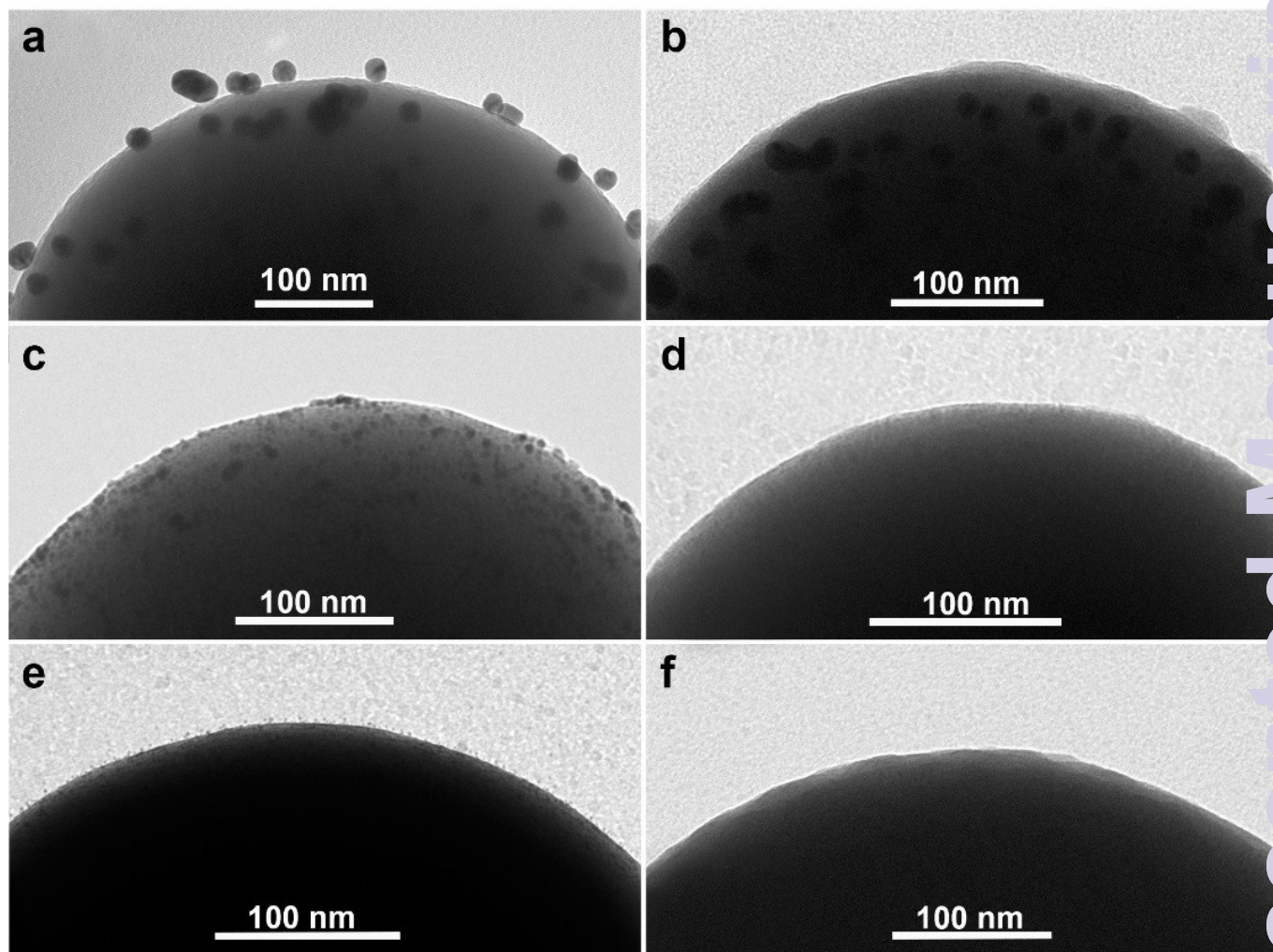


Figure 1. TEM images of the different AuNPs-based silica nanocomposites. (a) $\text{SiO}_2/14 \text{ nm-AuNPs}$; (b) $\text{SiO}_2/14 \text{ nm AuNPs/SiO}_2$; (c) $\text{SiO}_2/5.5 \text{ nm AuNPs}$; (d) $\text{SiO}_2/2.6 \text{ nm AuNPs/SiO}_2$; (e) $\text{SiO}_2/0.8\text{--}1.2 \text{ nm AuNPs}$; and (f) $\text{SiO}_2/0.8\text{--}1.2 \text{ nm AuNPs/SiO}_2$.

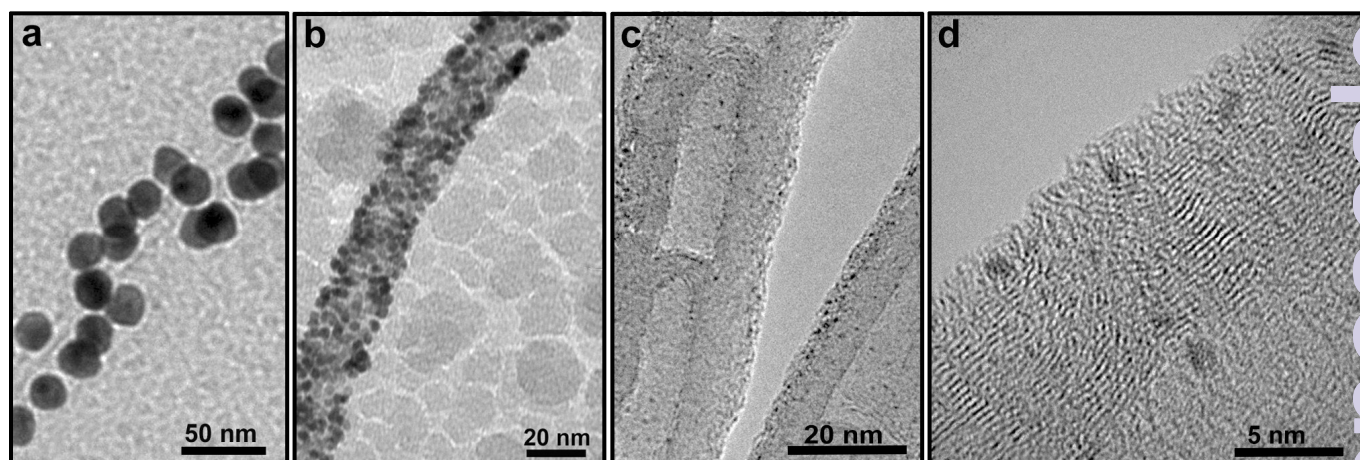


Figure 2. TEM images of the different MWCNT/AuNPs nanocomposites. (a) $\text{MWCNT}/13.80\pm 1.47 \text{ nm AuNPs}$; (b) $\text{MWCNT}/2.60\pm 0.64 \text{ nm AuNPs}$; (c) $\text{MWCNT}/0.8\text{--}1.2 \text{ nm AuNPs}$; and (d) HRTEM image of $\text{MWCNT}/0.8\text{--}1.2 \text{ nm AuNPs}$ (see also Figure S1 for energy-dispersive X-ray characterization of the clusters).

As expected from TEM imaging, the AuNPs embedded in the silica matrix produced little or no contrast between the metal nanoparticles and their support. In some cases, this lack of contrast gave rise to a featureless image. In view of these results, 14, 2.6, and 0.8–1.2 nm AuNPs were deposited or prepared onto multiwalled carbon nanotubes (MWCNTs) by following the experimental procedure applied when using silica beads as supports. As shown in Figure 2, TEM and HRTEM characterization confirmed the morphology of the pre-synthesized and *in situ* prepared AuNPs. In spite of this better contrast, silica beads were chosen as supports due to their higher thermal stability under normal atmospheric conditions compared to that of MWCNTs. As described in the literature, small metal nanoparticles supported in MWCNTs further coated with silica undergo a severe aggregation at high temperatures in air.¹⁸ This is due to the oxidation and thermal decomposition of carbon nanotubes under an O₂-rich atmosphere.

Having reached this point, the catalytic efficiency of the 14, 2.6, and 0.8–1.2 nm gold-containing nanostructures was evaluated. With this aim, the ferri/ferrocyanide couple was used as redox probe in the presence of the different nanocomposites in an aqueous solution containing sodium borohydride as reducing agent. Redox reactions were performed over a temperature range of 5–50 °C. NaBH₄ was always kept in large excess over K₃[Fe(CN)₆] ensuring pseudo-first-order conditions. Rates were measured by monitoring the decrease of hexacyanoferrate (III) absorption band at 420 nm (Figure 3, left). In all cases, the reactions were carried out in a highly basic medium (pH=13) in order to avoid NaBH₄ decomposition. The half-life times for all the catalyzed reactions were typically much shorter than that of the uncatalyzed process. The absorbance *versus* time data collected in this work always fitted satisfactorily to the integrated pseudo-first-order rate law, $A_t = A_\infty - (A_\infty - A_0) \exp(-k_{obs} t)$, (Figure 3, right) (see Supporting Information for further details).

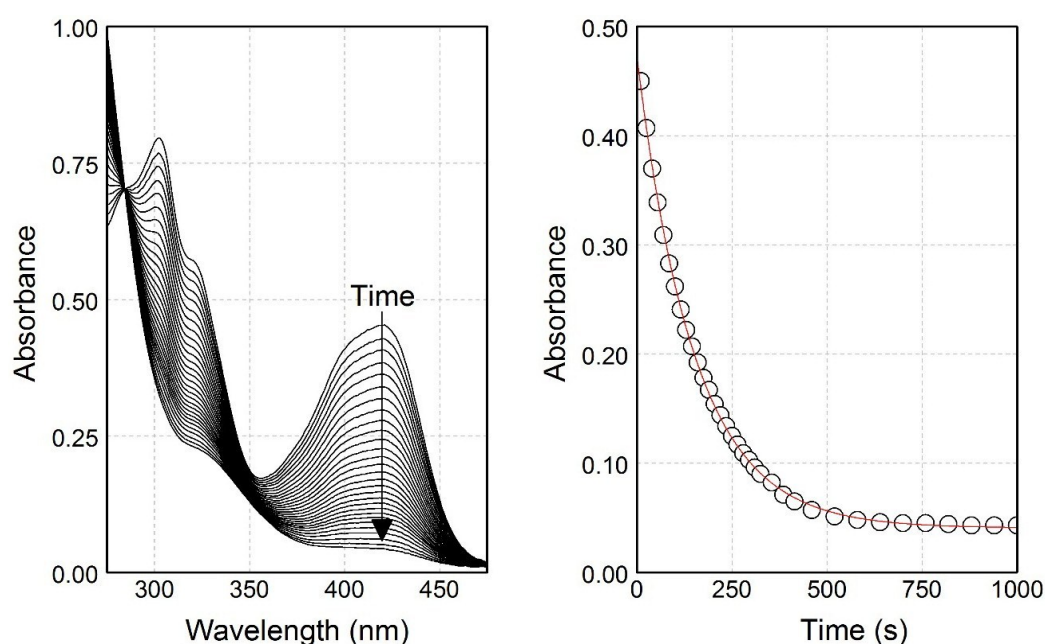


Figure 3. (left) Spectral evolution of ferricyanide in the presence of 2.6 nm AuNPs upon addition of sodium borohydride (some spectra omitted for clarity). T=50 °C; Reaction time= 1000 s. (right) Absorbance-time trace of ferricyanide reduction at 420 nm and fit to the integrated pseudo-first-order rate law (red line); $k_{obs} = (6.68 \pm 0.04) \times 10^{-3} \text{ s}^{-1}$.

As well documented in the literature,²⁰ catalysis of redox reactions in the presence of metal nanoparticles proceeds through an electrochemical mechanism in which the electron transfer occurs via nanoparticles. As known for this electron transfer, there is a large redox potential difference between the donor and acceptor species, which restrict the necessary passage of electrons. Nevertheless, the reaction becomes possible due to the intermediate redox potential of the AuNPs, which is in between the redox potential of the donor and the acceptor. In this way, the particles become anodic to the reducing agent and cathodic to the oxidizing species. Hence, the metal nanoparticles act as electron relay systems by transferring charges from borohydride ion to ferricyanide ion, thus helping the reaction to proceed. In fact, this redox transfer has been established as a benchmark test in order to assess the catalytic activity of metal nanoparticles in a wide range of nanoreactors.^{21–24}

After conducting the corresponding Arrhenius kinetic analysis (Figure S2), the values for the activation energy (E_a) of this Au-catalyzed process were estimated as 16.1 ± 0.6 , 15.1 ± 1.1 , and $10.4 \pm 1.0 \text{ kJ mol}^{-1}$ for the 14, 2.6 and 0.8–1.2 nm gold-containing architectures, respectively. The lowering of the activation and thus, the higher catalytic efficiency observed as particle size is decreased can be justified by the changes in the electronic properties of the particles due to the quantum size effects observed for nanoparticles below 2 nm in the presence of a large number of foreign ions.^{25–28} It must be noted that BH₄⁻ (used in great excess in all the catalytic experiments) is a strong nucleophile with a high electron injection capacity (redox potential -1.22 V vs NHE). Depending on the particle size, the donor capacity of borohydride may lead to a remarkable increase of the Fermi level of the particle or, in other words, to a shift of the redox potential of the particle toward more negative values. This variation in the Fermi level obeys the

expression $\Delta E_f = (2/3)E_f f$ where $f = (6r/R)\delta$, being r and R the atom and nanoparticles radius, respectively. Therefore, when dealing with ultra-small AuNPs a substantial variation of the Fermi level (ΔE_f) will take place. As a result, an increase in the difference between the resultant potential of the cluster and that of ferricyanide will be attained, that is, an increase in the overpotential.

In line with the above, it must be noted that under the working conditions the reduction of ferricyanide by borohydride is a surface-controlled reaction whose rate depends on the overpotential value according to the expression $rate \propto \exp((1-\alpha)\eta F/RT)$ where α is the transfer coefficient (typically, ~ 0.5), η is the overpotential, and F , R , T have their usual meanings. This expression, derived from the Butler-Volmer equation through its high field approximation,²⁹ shows the dependence of the reaction rate with the overpotential and therefore, with the size of the particle. As previously stated, η is directly related to the shift of the Fermi level which itself depends on the nanoparticle radius.³⁰ Thus, one should expect a greater catalytic activity per square nanometer when dealing with ultra-small AuNPs because the acute shift of the Fermi level in the sub-2 nm regime will lead to an important increase of the overpotential value. In light of the aforementioned, the observed decrease in the activation energy is given by the size-dependent redox properties of gold nanoparticles which in the end, control their role as electron relay systems.³¹ Thus, for a given concentration of AuNPs, the smaller their sizes, the more negative their redox potential. Ultimately, this shift will give rise to a larger potential difference between the metal particle and the oxidant (i.e., ferricyanide ion) and consequently, to a higher catalytic activity.³²

To further support such a claim, additional kinetic experiments were performed in the presence of 2.6 and 0.8–1.2 nm metal particles using the same gold concentration. In this situation, it is observed that the catalytic activity for the 0.8–1.2 nm clusters is much higher than that found for the 2.6 nm AuNPs (Table 1). On one hand, in the presence of 2.6 nm AuNPs the reaction conversion is only 12.5% after 30 min at room temperature. On the other hand, when using clusters as catalysts the reduction of ferricyanide to ferrocyanide is nearly complete after the same reaction time under identical experimental conditions. This remarkable acceleration cannot be justified by the higher surface-to-volume ratio in the presence of the gold clusters (ca. 2-fold increase in surface area compared to that of the 2.6 nm AuNPs). Therefore, these results provide evidence of a higher activity per square nanometer when dealing with ultra-small gold nanoparticles and hence, are indicative of the appearance of a lower activation energy.

Size (nm)	E_a (kJmol ⁻¹)	Yield (%)
2.6	15.1±1.1	12.5
0.8–1.2	10.4±1.0	94.0

Table 1. Activation energy and reaction yield for the reduction of ferricyanide ion by sodium borohydride in the presence of different-sized Au catalysts. Gold concentration was kept constant regardless the particle size. $[\text{NaBH}_4] = 0.01 \text{ M}$; $[[\text{Fe}(\text{CN})_6]^{3-}] = 5.0 \times 10^{-4} \text{ M}$; $T = 20 \text{ }^\circ\text{C}$; Reaction time = 1800 s.

At this stage, a series of annealing experiments were performed in order to assess the effect of different thermal treatments on the stability of the synthesized $\text{SiO}_2/\text{AuNPs}/\text{SiO}_2$ nanocomposites. Taking into account that the synthesis and stabilization of large AuNPs have been widely reported in the literature, efforts have been focused on the immobilization of the gold nanoclusters in the range below 3 nm. With this purpose, the silica-embedded 2.6 and 0.8–1.2 nm AuNPs were calcined in air at 100, 200, 300, 500 and 800 °C for 2 h, in the same muffle oven and next to each other. The treated samples were then analyzed by scanning transmission electron microscopy and UV/visible spectroscopy. As shown in Figure 4, no change in the size of the 2.6 nm gold nanoparticles was detected after thermal treatment. In the case of the Au clusters, the silica coating gave rise to a featureless image due to the lack of enough contrast. Nonetheless, the absence of distinguishable metal nanostructures after annealing seems to point out to an efficient stabilization of the gold nanoclusters. In the same vein, no surface plasmon band (SPB) was observed at 520 nm in the UV/Vis spectra of these samples. As known, for smaller particles where quantum effects are dominant, this feature is absent.²⁵ Therefore, the nonappearance of SPB also seems to point out to an efficient stabilization of the silica-embedded 2.6 and 0.8–1.2 nm AuNPs.

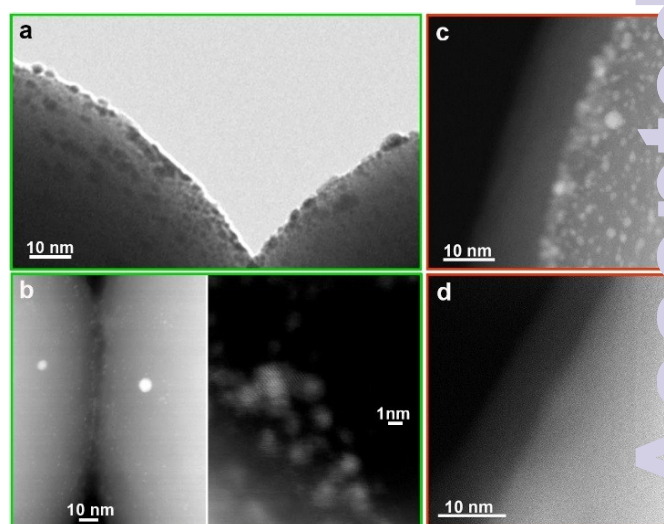


Figure 4. TEM (a) and HAADF-STEM images (b,c,d) of silica/gold and silica/gold/silica nanocomposites. (a) uncoated 2.6 nm AuNPs; (b) uncoated Au clusters; (c) silica-coated 2.6 nm AuNPs after thermal treatment at 800 °C, and (d) silica-coated Au clusters after thermal treatment at 800 °C.

Nevertheless, in order to shed more light on this issue, the catalytic efficiency of the 2.6 and 0.8–1.2 nm gold nanoparticles was assessed after the different calcination treatments through the estimation of E_a for the redox reaction of the ferri/ferrocyanide couple. These data are summarized in Figure 5.

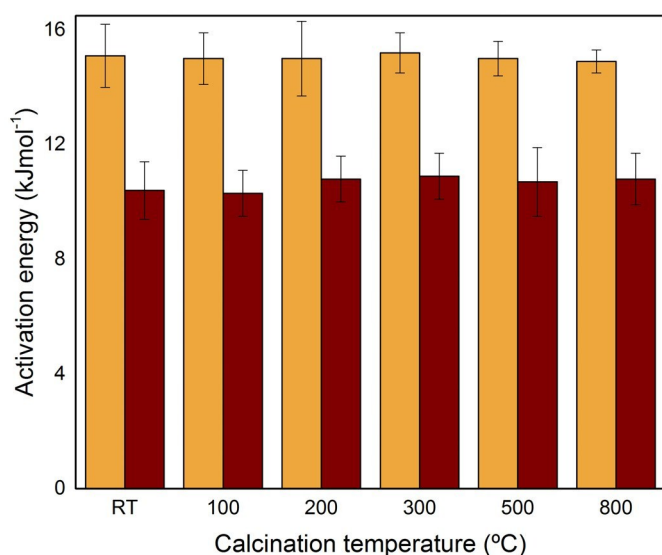


Figure 5. Activation energy for the Au-catalyzed reduction of hexacyanoferrate (III) by sodium borohydride for 2.6 nm Au nanoparticles (orange) and 0.8–1.2 nm gold nanoclusters (brown) before and after calcination at different temperatures.

As shown, E_a remains constant for a given nanoparticle size regardless the temperature at which the samples are calcined. Thus, an average activation energy of $15.0 \pm 0.4 \text{ kJmol}^{-1}$ is obtained for the redox process in the presence of 2.6 nm AuNPs while an average E_a of $10.6 \pm 0.4 \text{ kJmol}^{-1}$ is achieved for the reaction catalyzed by 0.8–1.2 nm AuNPs. Since the activation energy for the non-catalyzed reaction is 30 kJmol^{-1} ,³³ the obtained results point out to a remarkable and stable catalytic activity of these hybrid composites regardless the temperature at which the metal nanoparticles are calcined. In this regard, the estimation of activation energy, understood as the minimum energy required to reach the transition state for a given reaction, constitutes an efficient criterion in order to evaluate the status of a catalyst in the $\sim 1 \text{ nm}$ regime. In this case, this energy barrier depends on the intrinsic reactivity of the reactant species at the low-coordinated gold atoms (corner or edge positions) where the catalyzed reaction occur, which itself depends on interrelated factors such as size, shape and quantum effects of metal nanoparticles.³⁴ In this way, variations in the magnitude of activation energy after chemical or thermal treatment are associated to changes in reactivity and hence, related to morphological alterations in the catalytic material. As a result, the steadiness of E_a for the reduction of ferricyanide ion involves that the Fermi level of the Au clusters remains unchanged after annealing and therefore, that their size is well-preserved.

A major advantage of using activation energy as criterion of cluster stability lies in the intensive character of this parameter. In this respect, E_a is independent of the gold concentration and therefore, free from cumulative errors that may arise from preparing and handling the extremely small amounts of catalytic material used in this case. In the same way, it is also important to note the influence that calcination exerts on the catalytic activity of these particles. Along these lines, the reaction rate undergoes an important increase for a given amount of clusters as calcination temperature

is raised. As previously mentioned, harsh thermal conditions are usually employed in order to remove organic capping agents allowing reactants to better access to the catalyst active sites. Hence, this higher rates can be ascribed to the increasing removal of the citrate ions chemisorbed on the cluster surface as annealing temperature is raised. For that reason, the determination of E_a constitutes an applicable benchmark of comparison with regard to the intrinsic catalytic efficiency of nanoclusters in contrast to reaction rates or yields for a given time.

The obtained results point out to the absence of sintering and structural changes in the SiO_2 -embedded clusters described here, even under rather harsh conditions. It must be noted that the temperature reached in this treatment is well-above the so-called Tammann temperature of bulk gold ($395 \text{ }^\circ\text{C}$).³⁵ This parameter, defined as $T_{\text{Tammann}} = 0.5T_F$ (T_F representing the melting point), is often used as a rule of thumb in order to describe the conditions at which sintering becomes particularly noticeable. The above expression evidences the key role that melting point plays in the aggregation-resistant properties of metal catalysts. This issue is especially relevant when dealing with ultra-small metal nanoparticles given that their large surface-to-volume ratio leads to dramatic changes in their thermal properties compared to those of the bulk material. Thus, the melting point for 2 nm AuNP is predicted to be around $327 \text{ }^\circ\text{C}$ which significantly lowers the energetic requirements for sintering to take place ($T_F = 163 \text{ }^\circ\text{C}$).³⁶ In the present case, such a suppression in the T_F justifies the need of further immobilization than that provided by the mere deposition of the gold nanoclusters onto the silica beads. In this respect, it is observed that small changes in the synthetic procedure of the $\text{SiO}_2/0.8\text{--}1.2 \text{ nm AuNPs}$ lead to variations in the morphology of these nanoclusters. Thus, when the excess of unreacted species is removed by successive centrifugation/stirring-driven redispersion cycles the activation energy of the $\text{SiO}_2/0.8\text{--}1.2 \text{ nm AuNPs}$ is estimated as $10.6 \pm 1.2 \text{ kJmol}^{-1}$. This value is in good agreement with those obtained for the $\text{SiO}_2/0.8\text{--}1.2 \text{ nm AuNPs/SiO}_2$ composites after different thermal treatments. Conversely, during the redispersion of $\text{SiO}_2/0.8\text{--}1.2 \text{ nm AuNPs}$ a mere 3-second lasting mild ultrasonic irradiation rises E_a to $15.9 \pm 0.7 \text{ kJmol}^{-1}$. This higher value corresponds to larger particles where quantum size effects are not present. Therefore, the observed increase in the energy barrier (Figure S3) can be attributed to an ultrasound-driven sintering process between the 0.8–1.2 nm AuNPs deposited on the silica beads. It must be noted that the irradiation of a liquid sample with ultrasonic waves ($>20 \text{ kHz}$) gives rise to alternating high-pressure and low-pressure cycles. Such cycles create small vacuum bubbles or voids in the liquid, which then collapse violently (cavitation) generating rather high local temperatures. For this reason, stirring (and not sonication) was employed along the synthesis of the $\text{SiO}_2/\text{AuNPs}$ composites so sintering of the metal particles deposited on the silica support could be mitigated. The use of ultrasonic irradiation and/or stirring becomes irrelevant after the silica coating is applied to yield a $\text{SiO}_2/0.8\text{--}1.2 \text{ nm AuNPs/SiO}_2$ structure. In this case, the preservation of the catalytic activity confirms the attainment of a noteworthy stabilization through this configuration.

Having reached this point, it seems clear that this synthetic approach is ideally suited to endow gold nanoclusters with a high thermal stability. This remarkable resistance to sintering can be additionally exploited for the fabrication of hollow nanostructures, a process that usually involves the thermal removal of an organic compartment in order to form the inner cavity and even induce pore formation in the protecting shell. In this regard, it must be noted that hard template methods are the most frequently used procedures for the synthesis of voided spheres and rattle-like nanostructures due to its relative simplicity.³⁷ The benefits of creating nanocavities in order to further exploit the potential of functional metal nanomaterials has been recently reviewed by our group.³⁸

In this scenario, the stability of the gold nanoclusters has been assessed through the synthesis and application of the hollow counterparts of the $\text{SiO}_2/0.8\text{--}1.2\text{ nm AuNPs}/\text{SiO}_2$ nanocomposites.

With this aim, polystyrene (PS) beads were used as sacrificial templates and coated with a microporous silica layer (~1-nm pore size) onto which 0.8–1.2 nm AuNPs were subsequently deposited. These clusters were further coated with a mesoporous silica layer (2–3-nm pore size). In this way, the nature of the silica shells can be tuned regardless of each other's porosity and the size of the embedded metal nanoparticles. Finally, the hollow nanocomposites were obtained by calcination of the PS beads at 550 °C (see Supporting Information for further details). As shown in Figure 6, the distinctive morphology of the silica layers is well preserved after this thermal treatment. As can be noted, the vertical pore orientation obtained in the mesoporous coating clearly contrasts with the more compact microporous layer. The radial orientation of the mesopores is explained on the basis of the preferred alignment of CTAB micelles normal to a growth surface.³⁹

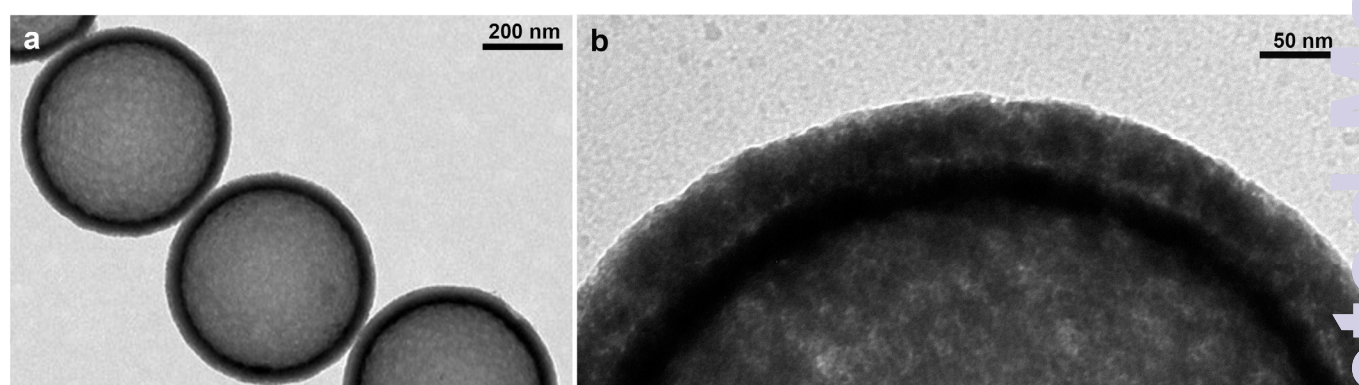
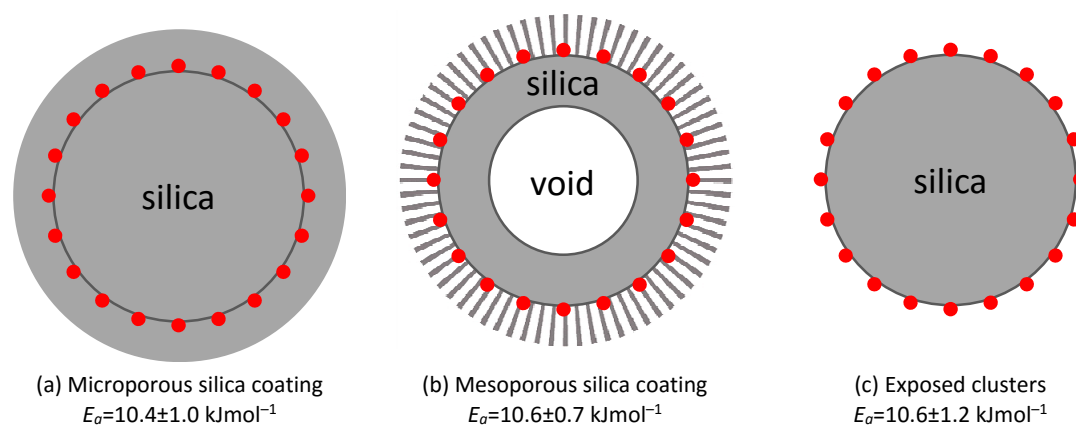


Figure 6. TEM images of (a) void/microporous silica layer (20-nm thickness)/Au clusters/mesoporous silica layer (30-nm thickness) nanocomposite; and (b) zoomed-in image showing the preservation of the distinctive porosity of the silica shells after calcinating at 550 °C.

Following the calcination of the PS beads, the stability of the encapsulated gold nanoclusters was kinetically evaluated by using the ferri/ferrocyanide couple as redox probe. In this case, the activation energy for this Au-catalyzed process was estimated as $10.6 \pm 0.7\text{ kJmol}^{-1}$. This result matches those obtained for the

different architectures reported herein (Scheme 2). This good agreement confirms the preservation of the highly catalytic properties of these materials after the thermal removal of the sacrificial core and therefore, the efficient immobilization of the Au nanoclusters.



Scheme 2. Representation and values for of (a) silica bead/Au clusters/microporous silica layer nanocomposite; (b) void/microporous silica layer/Au clusters/mesoporous silica layer nanocapsule, and (c) silica bead/Au clusters nanostructure.

The nanoreactors synthesized herein take advantage of all the benefits inherent to the use of silica, such as its thermal stability, chemical inertness, optical transparency, size sieving capabilities,⁴⁰ as well as its many available synthetic methods.⁴¹ Moreover, the mesoporous shell of the nanoreactor may efficiently enhance the adsorption of different molecules from the bulk solution and enrich their presence in the void, leading to a higher local concentration in the inner cavity and thus, to a greater catalytic performance compared to that found in their core-shell counterparts.⁴² A further asset of these architectures is their easy dispersibility in organic as well as aqueous solvents, among which simulated body fluids are of particular importance. As shown in Figure S4, colloidal Au nanoparticles easily aggregate in this kind of media. The same applies to Au nanoparticles supported onto silica beads where a fast decantation and aggregation is observed in SBF (Figure S5). These results further justify the need for architectures that endow metal nanostructures with an enhanced stability in complex environments. In this regard, dynamic light scattering measurements (Figure S6) confirm the stability of the nanocapsules in these plasma-mimicking solutions and thus, an efficient immobilization of the catalytic material located therein. All these findings open the door to the use of these hollow nanocomposites in biomedical-related applications.

Conclusions

A synthetic strategy for the stabilization of Au nanoparticles as small as 0.8 nm is reported. In this case, gold nanoclusters are embedded between two different silica shells that can be tuned regardless of each other's porosity and the size of the metal nanoparticles. Through this configuration an outstanding compromise between immobilization and accessibility to the metal nanocatalyst can be met. This is evidenced by the preservation of the catalytic properties of these materials which remain intact after exposure to a thermal treatment of up to 800 °C. Together with this extreme thermal stability, these nanoreactors are found to dispersible and stable in different organic and aqueous solvents including SBF. This great versatility endows these nanoreactors with a promising potential regarding their application under realistic technical conditions.

Acknowledgements

This work was funded by Xunta de Galicia (INBIOMED-FEDER "unha maneira de facer Europa" and EM2014/035), Fundación Ramón Areces, Fundación Tatiana Pérez de Guzmán el Bueno, and European Union Seventh Framework Programme [FP7/REGPOT-2012-2013.1] under Grant Agreement no. 316265, BIOCAPS. The scanning transmission electron microscopy (STEM) studies were conducted at Laboratorio de Microscopías Avanzadas (LMA) at Instituto de Nanociencia de Aragón (INA) - Universidad de Zaragoza (Spain). The STEM measurements were supported by European Union Seventh Framework Program under Grant Agreement 312483-ESTEEM2 (Integrated Infrastructure Initiative-I3). R.A. acknowledges funding from MINECO-Spain (FIS2013-46159-C3-3-P) and EU-H2020 project ITN-Enabling Excellence (Grant Number 642742).

References

- 1 M. Stratakis and H. Garcia, *Chem. Rev.*, 2012, **112**, 4469–4506.
- 2 Y. Zhang, X. Cui, F. Shi and Y. Deng, *Chem. Rev.*, 2011, **111**, 2467–2505.
- 3 A. Corma and H. Garcia, *Chem. Soc. Rev.*, 2008, **37**, 2076–2126.
- 4 A. S. K. Hashmi and G. J. Hutchings, *Angew. Chem. Int. Ed.*, 2006, **45**, 7896–936.
- 5 T. W. Hansen, A. T. DeLaRiva, S. R. Challa and A. K. Datye, *Acc. Chem. Res.*, 2013, **46**, 1720–1730.
- 6 C. T. Campbell, *Acc. Chem. Res.*, 2013, **46**, 1712–1719.
- 7 J. A. Lopez-Sanchez, N. Dimitratos, C. Hammond, G. Brett, L. Kesavan, S. White, P. Miedziak, R. Tiruvalam, R. Jenkins, A. F. Carley, D. Knight, C. J. Kiely and G. J. Hutchings, *Nat. Chem.*, 2011, **3**, 551–556.
- 8 S. J. Tauster, S. C. Fung, R. T. K. Baker and J. A. Horsley, *Science*, 1981, **211**, 1121–1125.
- 9 T. Zhang, H. Zhao, S. He, K. Liu, H. Liu, Y. Yin and C. Gao, *ACS Nano*, 2014, **8**, 7297–7304.
- 10 E. D. Martínez, C. Boissière, D. Grosso, C. Sanchez, H. Troiani and G. J. A. A. Soler-Illia, *J. Phys. Chem. C*, 2009, **113**, 13137–13151.
- 11 Z. Liu, R. Che, A. A. Elzatahry and D. Zhao, *ACS Nano*, 2014, **8**, 10455–10460.
- 12 P. Botella, A. Corma and M. T. Navarro, *Chem. Mater.*, 2007, **19**, 1979–1983.
- 13 S. H. Joo, J. Y. Park, C.-K. Tsung, Y. Yamada, P. Yang and G. A. Somorjai, *Nat. Mater.*, 2009, **8**, 126–131.
- 14 L. Alves, B. Ballesteros, M. Boronat, J. R. Cabrero-Antonino, P. Concepción, A. Corma, M. A. Correa-Duarte and I. Mendoza, *J. Am. Chem. Soc.*, 2011, **133**, 10251–10261.
- 15 J. Turkevich, P. C. Stevenson and J. Hillier, *Discuss. Faraday Soc.*, 1951, **11**, 55–75.
- 16 D. G. Duff, A. Baiker and P. P. Edwards, *Langmuir*, 1993, **9**, 2301–2309.
- 17 Z. Chen, Z.-M. Cui, P. Li, C.-Y. Cao, Y.-L. Hong, Z. Wu and W.-G. Song, *J. Phys. Chem. C*, 2012, **116**, 14986–14991.
- 18 C. Mateo-Mateo, C. Vázquez-Vázquez, M. Pérez-Lorenzo, V. Salgueiriño and M. A. Correa-Duarte, *J. Nanomater.*, 2012, 404159.
- 19 P. R. Van Rhee, M. J. McKelvy and W. S. Glaunsinger, *J. Solid State Chem.*, 1987, **67**, 151–169.
- 20 A. Henglein, *J. Phys. Chem.*, 1993, **97**, 5457–5471.
- 21 P. Hervés, M. Pérez-Lorenzo, L. M. Liz-Marzán, J. Dzubiella, Y. Lu and M. Ballauff, *Chem. Soc. Rev.*, 2012, **41**, 5577–5587.
- 22 M. Sanlés-Sobrido, M. Pérez-Lorenzo, B. Rodríguez-González, V. Salgueiriño and M. A. Correa-Duarte, *Angew. Chem. Int. Ed.*, 2012, **51**, 3877–3882.
- 23 M. Sanlés-Sobrido, M. A. Correa-Duarte, S. Carregal-Romero, B. Rodríguez-González, R. A. Álvarez-Puebla, P. Hervés and L. M. Liz-Marzán, *Chem. Mater.*, 2009, **21**, 1531–1535.
- 24 S. Carregal-Romero, J. Pérez-Juste, P. Hervés, L. M. Liz-Marzán and P. Mulvaney, *Langmuir*, 2009, **26**, 1271–1277.
- 25 M.-C. Daniel and D. Astruc, *Chem. Rev.*, 2003, **104**, 293–346.
- 26 H. Qian, M. Zhu, Z. Wu and R. Jin, *Acc. Chem. Res.*, 2012, **45**, 1470–1479.

- 27 U. K. M. Vollmer, *Optical Properties of Metal Clusters*, 1995.
- 28 T. K. Sau, A. Pal and T. Pal, *J. Phys. Chem. B*, 2001, **105**, 9266–9272.
- 29 A. K. N. Bockris, J. O. M.; Reddy, *Modern electrochemistry*, Plenum Press, NY, Ed.; 1977.
- 30 N. R. Jana and T. Pal, *Langmuir*, 1999, **15**, 3458–3463.
- 31 A. Henglein, *Chem. Rev.*, 1989, **89**, 1861–1873.
- 32 L. Bard, A.; Faulkner, *Electrochemical methods: fundamentals and applications*, Wiley-VCH; NY, Ed.; 2001.
- 33 T. Freund, *J. Inorg. Nucl. Chem.*, 1959, **9**, 246–251.
- 34 M. Boronat, A. Leyva-Pérez and A. Corma, *Acc. Chem. Res.*, 2014, **47**, 834–844.
- 35 A.-F. An, A.-H. Lu, Q. Sun, J. Wang and W.-C. Li, *Gold Bull.*, 2011, **44**, 217–222.
- 36 P. Buffat and J.-P. Borel, *Phys. Rev. A*, 1976, **13**, 2287–2298.
- 37 M. Priebe and K. M. Fromm, *Chem. Eur. J.*, 2015, **21**, 3854–3874.
- 38 B. Vaz, V. Salgueiriño, M. Pérez-Lorenzo and M. A. Correa-Duarte, *Langmuir*, 2015, **31**, 8745–8755.
- 39 B. Tan and S. E. Rankin, *J. Phys. Chem. B*, 2004, **108**, 20122–20129.
- 40 Z.-A. Qiao, P. Zhang, S.-H. Chai, M. Chi, G. M. Veith, N. Gallego, M. Kidder and S. Dai, *J. Am. Chem. Soc.*, 2014, **136**, 11260–11263.
- 41 H. E. Bergna and W. O. Roberts, *Colloidal silica: fundamentals and applications*, CRC Press; FL, Ed.; 2006.
- 42 Z.-M. Cui, Z. Chen, C.-Y. Cao, L. Jiang and W.-G. Song, *Chem. Commun.*, 2013, **49**, 2332–2334.